Nano Research
2020, 13(5): 1369–1375

ISSN 1998-0124 CN 11-5974/O4
https://doi.org/10.1007/s12274-020-2634-y

Research Article

Complementary doping of van der Waals materials through controlled intercalation for monolithically integrated electronics

Ming Ke, Huu Duy Nguyen, Hang Fan, Man Li, Huan Wu, and Yongjie Hu (✉)

School of Engineering and Applied Science, University of California, Los Angeles, California 90095, USA

Received: 5 November 2019 / **Revised:** 29 December 2019 / **Accepted:** 31 December 2019

ABSTRACT

Doping control has been a key challenge for electronic applications of van der Waals materials. Here, we demonstrate complementary doping of black phosphorus using controlled ionic intercalation to achieve monolithic building elements. We characterize the anisotropic electrical transport as a function of ion concentrations and report a widely tunable resistivity up to three orders of magnitude with characteristic concentration dependence corresponding to phase transitions during intercalation. As a further step, we develop both p-type and n-type field effect transistors as well as electrical diodes with high device stability and performance. In addition, enhanced charge mobility from 380 to 820 $cm^2/(V{\cdot}s)$ with the intercalation process is observed and explained as the suppressed neutral impurity scattering based on our *ab initio* calculations. Our study provides a unique approach to atomically control the electrical properties of van der Waals materials, and may open up new opportunities in developing advanced electronics and physics platforms.

KEYWORDS

nanoelectronics, two-dimensional (2D) materials and heterostructures, field-effect transistors (FETs), diode, tunable properties, black phosphorus

1 Introduction

The scaling down and increasing power of modern technology components has motivated extensive studies during the last decades on the synthesis and integration of nanomaterials including nanowires [1–10], nanotubes [11–20], nanocrystals [21–26], and van der Waals materials [27–37]. For electronics, doping control is key to developing building blocks and functional circuits. However, traditional doping techniques such as ion implantation routinely used in silicon industry may not be directly applicable to nanomaterials, in particular van der Waals materials due to their peculiar structures [38–40]. Intensive efforts have been made recently in developing effective doping methods such as chemical surface modifications [41–43], atomic substitutions [44–46], gating [47–49], and layer stacking [50–53] in the aim to improve the doping controllability, performance stability, and processing flexibility.

In this work, we demonstrate complementary doping of two-dimensional (2D) materials using ionic intercalation for monolithically integrated electronics. Using black phosphorus (BP) as a model system, we develop both p-type and n-type transistors as well as electrical diodes as the basic electronic building elements. BP crystals were synthesized using the chemical vapor deposition method. Red phosphorus was used as the reaction source with SnI_4 and Sn as the mineralizer. The detailed synthesis procedure was reported in our recent publications [54, 55]. BP has a puckered orthorhombic crystal structure of P atoms [56] (Fig. 1(a)). Inside a 2D layer, each P atom forms covalent bonds from the 3p orbitals: A longer bond connects the P atoms in the top and bottom planes, and a shorter bond connects the nearest P atoms of the same plane. The interlayer interaction is based on van der Waals bonding. Therefore, BP has three characteristic directions denoted as the armchair (AC), zigzag (ZZ), and cross-plane (CP), which give rise to their anisotropic properties [57] such as thermal conductivity [55, 58], and interface boundary resistance [54]. The crystal orientation of the BP is identified using angle-resolved Raman spectroscopy (Fig. 1(b)): Three of the six Raman vibrational modes can be detected with laser incident along the cross-plane direction following the symmetric selection rule [59]. The three distinctive peaks appearing at 363, 440, and 467 cm^{-1} represent the vibration modes A_g^1, B_{2g}, and A_g^2, respectively. Note that the intensity of the Raman peaks evolves with respect to the alignment of the Raman polarization with respect to the crystal orientation [54, 60]. For example, the maximum intensity of the A_g^2 peak corresponds to the alignment along the AC-direction (i.e. denoted as 0° in Fig. 1(b)). The B_{2g} peak is maximized when the polarization is aligned precisely 45° between the AC- and ZZ-direction. Therefore, the Raman spectra data are used to identify the crystal orientations of the BP samples used in the following anisotropic electrical measurements. We also note that Raman measurements taken at various locations on the samples show consistent results, indicating the uniform crystalline quality of the sample.

2 Experimental

To control the doping concentration through intercalation, we design a lithium ion battery device that allows electrochemical intercalation of Li into BP (Fig. 1(a)). Thin film BP crystals with clean and smooth surfaces are prepared using mechanical exfoliation to serve as the cathode of the electrochemical system.

Address correspondence to yhu@seas.ucla.edu

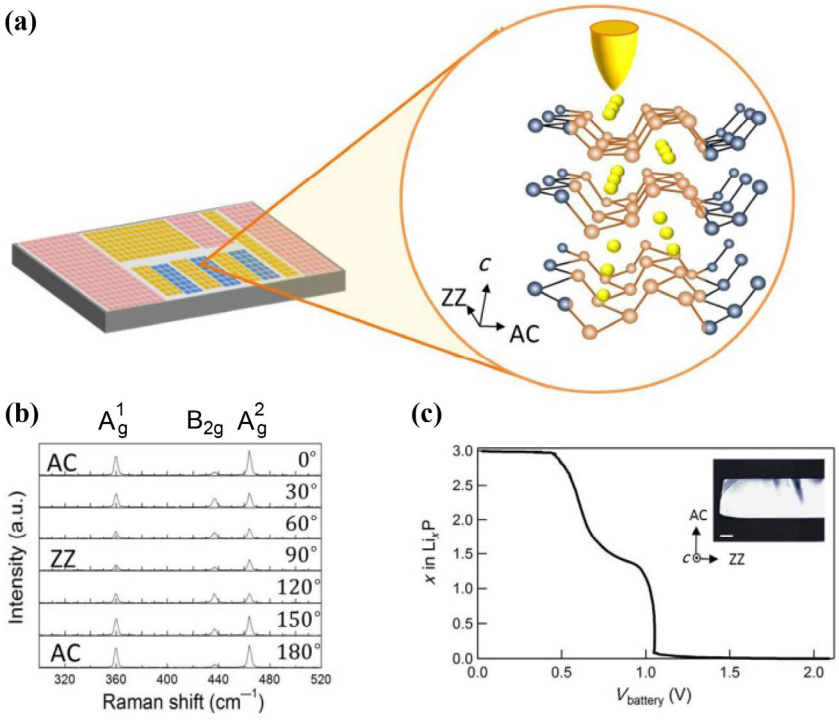

Figure 1 Controlled ionic intercalation to achieve complementary doping of van der Waals materials. (a) Schematic illustrating the electrochemical control for local ionic intercalations in black phosphorus (BP). The AC-, ZZ-, and *c*-axis denote the armchair, zigzag, and cross-plane directions, respectively. (b) Angle resolved Raman spectroscopy of BP. The intensity of the three visible vibration modes are measured and used to determine the principle directions of BP. (c) Galvanostatic discharge curve for the lithium-BP devices. Inset shows the optical image of a rectangular thin film black phosphorus sample. Scale bar is 100 μm.

Doping of the BP sample through ionic intercalation is carefully controlled by applying a localized potential using a metal probe tip. The battery composes of a Li pellet metal (MTI Corp.) as the reference electrode and 1 M $LiPF_6$ salt in 1:1 w/w EC/DEC (Sigma Aldrich) as the electrolyte. More details regarding device fabrication and the *in-situ* electrochemical setup can be found in our recent publication [55]. A typical galvanostatic discharge of the BP battery discharge potential versus lithium concentration (represented by x in Li_xP) is shown in Fig. 1(c). Starting from the pristine BP with $x = 0$, discharging drives more lithium intercalation into Li_xP electrode and ends at the fully discharged state with $x = 3$. Note that there are three main structural phases for Li_xP [61, 62]. For low ion concentration ($0 \leq x \leq 0.3$), the intercalation mainly involves physical intercalation and the delithiation is highly reversible. Further discharge will induce irreversible P–P bond breaking and alloying effects [63], corresponding to a potential drop and then a wide plateau in the voltage window ($0.3 < x < 2.6$). Discharging beyond induces phase change; at this point, the electrode becomes a mixture of Li_2P and Li_3P.

3 Results and discussion

We first measured the electrical transport along the cross-plane direction as a function of lithium concentrations (i.e. x in Li_xP). Parallel metal electrodes are deposited on the top and bottom surfaces of the BP sample to distribute the electric flux uniformly (inset, Fig. 2(a)). The cross-plane resistivity ($\rho_\perp$) of pristine BP is measured to be 650 $\Omega \cdot$cm, in agreement with reported values in Ref. [64]. With ionic intercalation, the measured cross-plane resistivity of Li_xP shows a monotonic and gradual decrease from pristine BP to Li_3P, as expected from the increased doping that leads to the higher concentration of carriers (Fig. 2(a)). Simultaneously, the in-plane electrical transport across the Li_xP is also reported (inset, Fig. 2(b)). In contrast, the in-plane resistance ($R_{//}$) shows a step-wise decrease with increasing lithium concentrations but maintains minute changes within each crystal phase. $R_{//}$ drops by over an order of magnitude at the lithium concentrations corresponding to the phase transitions as identified by the galvanostatic discharge measurement shown in Fig. 1.

To determine the anisotropic in-plane electrical resistivity ($\rho_{//}$) of lithium intercalated BP, we performed four-terminal Van der Pauw measurement. In general, the anisotropic electrical resistance is described by a second-rank tensor, defined in terms of the vector electrical field intensity and the vector current density. For BP and intercalated BP system, the tensor is symmetrical and reduces to three parameters. The principal directions of the resistivity tensor are previously identified from the Raman measurements. Therefore, the in-plane resistivity tensor can be determined by measuring the voltage–current ratios of a rectangular sample (Fig. 3) [65]. First, in-plane measurements are taken on a rectangular sample: $R_{12,34} = V_{12} / I_{34}$ and $R_{13,24} = V_{13} / I_{24}$ are measured by placing voltage and current probes on two adjacent electrodes indicated by their respective subscripts at opposing ends (inset, Fig. 3(a)). Then a similar measurement is made with all connections rotated by a quarter turn (Fig. 3(a)). The previously measured cross-plane resistivity ($\rho_\perp$) of Li_xP (Fig. 2(a)) is used as input for the analysis. From multiple measurements and using the analysis model to map the anisotropic solid to an equivalent isotropic solid [65], $\rho_{//}$ along the ZZ- and AC-direction are determined (Fig. 3(c)). To verify the measurement accuracy, we use the determined equivalent isotropic resistivity, sample length, and width to reconstruct the equivalent isotropic solid and predict the current response, which is subsequently compared with the direct measurement on the anisotropic sample (Fig. 3(b)). The measurement and modeling results of the *I*–*V*

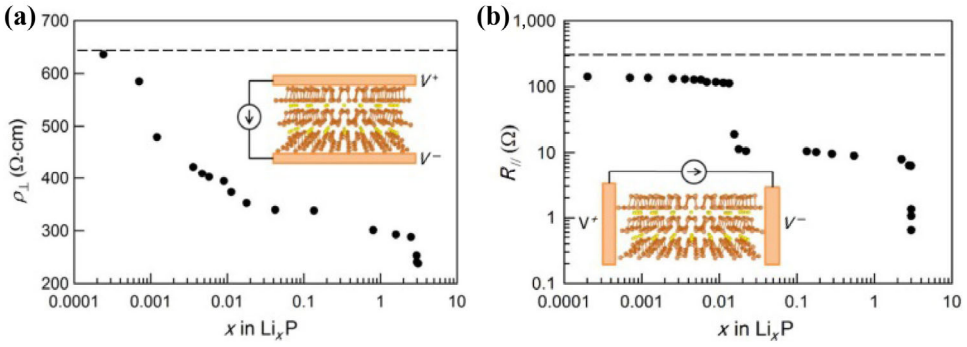

Figure 2 Two-terminal electrical measurement and cross-plane electrical resistivity. (a) Ionic concentration dependent cross-plane resistivity ($\rho_\perp$). Dashed line indicates the pristine BP value. Inset, schematic illustrates the cross-plane measurement configuration. (b) Ionic concentration dependent in-plane resistance ($R_{//}$) of thin film BP. Dashed line indicates the pristine BP value. Inset, schematic illustrats the in-plane measurement configuration.

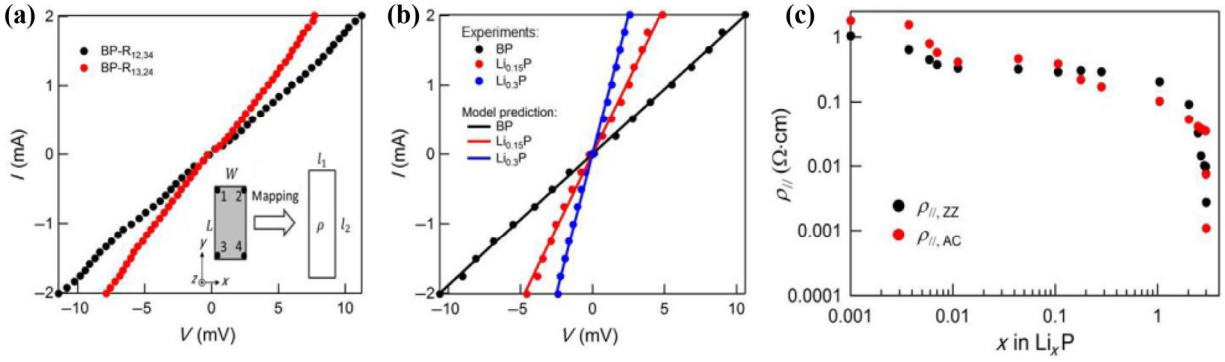

Figure 3 Four-terminal electrical measurement and anisotropic in-plane electrical resistivity. (a) Van der Pauw measurement of the resistance (R), determined by the ratio of voltage between two adjacent electrodes to the current between the other two electrodes. Inset, schematic illustrates the notations for R, sample dimensions, as well as the measurement concept of mapping transformation between the real anisotropic sample to the equivalent imaginary solid with isotropic resistivity (ρ). (b) Simulated response current (I–V) based on the equivalent solid model, in comparison to the experimental measurement. (c) Measurement results of the in-plane electrical resistivity as a function of ionic concentrations, in the AC- and ZZ-directions.

curves of $R_{12,34}$ for different samples (the pristine BP, $Li_{0.15}P$, and $Li_{0.3}P$) show very good agreement and indicate the modeling assumption is valid for our experiment. From these measurements, the in-plane electrical resistivity of pristine BP in the ZZ- and AC-directions are found to be 0.89 and 1.12 Ω·cm, respectively, consistent with literature values [66, 67]. Furthermore, measurements are performed for Li_xP of different lithium concentrations with x from 0 up to 3. The measured in-plane resistivity along ZZ- and AC-directions as a function of lithium concentrations are plotted in Fig. 3(c), showing a continuous reduction in resistivity with increased intercalation level. Similar to the cross-plane resistivity, there is a plateau corresponding to the steady discharge window and phase transitions.

Next, we develop electrical diode device based on the demonstrated complementary doping. Spatially controlled doping is achieved using ebeam lithography defined patterning [10, 68]. For example, a diode junction is formed at the interface between pristine BP and $Li_{0.7}P$ (Fig. 4(a)). Under the optical image, there is a distinct contrast indicating a clear interface: $Li_{0.7}P$ shows up in a dark brown in color, which has been attributed to intercalation induced phase transition and has been observed in other systems such as lithiated MoS_2 [69]. The difference in the Fermi levels across this heterogeneous interface forms a potential barrier (Φ) and is expected to introduce non-linear electrical transport [70]. Our experimental measurements of such diode devices from pristine BP to $Li_{0.3}P$ (Fig. 4(b)) verify such expectation: The I_{ds}–V_{ds} curves evolve

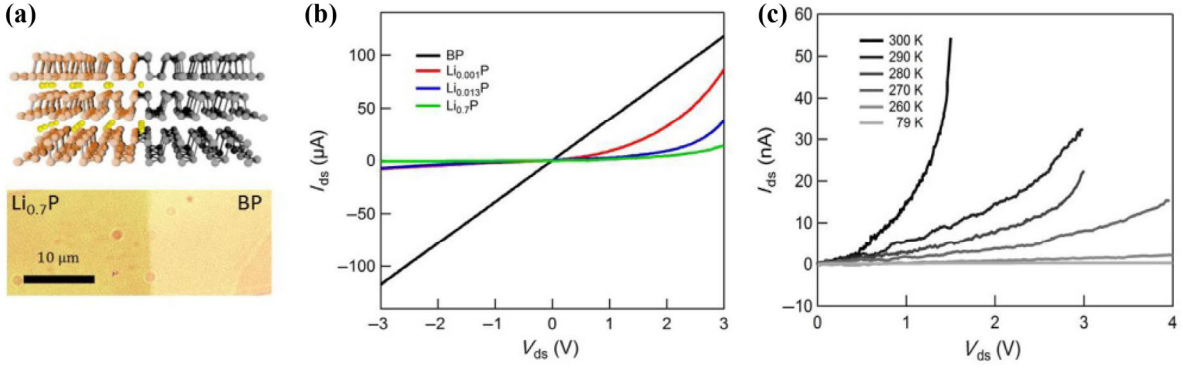

Figure 4 Diode device and transport characterizations. (a) Schematic illustrating the formation of a diode through ionic intercalation, and optical image of a BP-$Li_{0.7}P$ diode device with the clear interface shown by optical contrast. (b) I_{ds}–V_{ds} data for BP-Li_xP devices with different ionic concentrations. (c) Temperature dependent I_{ds}–V_{ds} data measured for a fully intercalated BP diode device.

from linear to nonlinear and show an increased rectification effect for higher lithium concentrations. When a positive bias is applied to the diode, the Fermi energy (for holes) of the Li_3P is lowered with respect to the Fermi energy in the BP which results in a smaller potential drop across the junction. The balance between diffusion and drift is disturbed and more holes will diffuse towards the Li_3P than the number drifting into the BP. This leads to a positive current through the junction at a voltage comparable to the potential height. When a negative voltage is applied, the Fermi energy of the Li_3P is raised and now the potential across the BP now increases and further restricts the hole transport to the Li_3P, so that the flow of holes is limited by that barrier. As a result, this Li_3P-BP junction with positive barrier height has a pronounced rectifying behavior. A large current exists under forward bias, while almost no current exists under reverse bias. In addition, the measurement shows a gradual increase in the threshold voltage of V_{ds} from around 1 to ~ 2 V with increased doping concentrations corresponding to increased barrier height. We further measure the temperature dependent transport of the diode from 300 to 79 K (Fig. 4(c)). The diode current reduces with lowering temperature due to the suppressed thermal energy of charge carriers. The barrier potential extracted from transport measurement is ~ 0.1 V for Li_3P and note that this barrier potential remains consistent throughout the whole temperature range, indicating high stability of the intercalation doping.

As a further step, we develop both p-type and n-type field-effect transistors (FETs) based on complementary intercalation doping. For p-type devices, lithium intercalated BP is used as the semiconductor channel. The devices are fabricated using HfO_2 high-κ gate dielectrics through atomic layer deposition and metal top gate electrodes. More details regarding the fabrication have been reported previously [8, 71, 72]. Typical output and transfer characteristics recorded from the pristine and intercalation devices are show in Fig. 5. The I_{ds}–V_{ds} curves of BP and Li_xP devices show that the drain current I_{ds} increases linearly with V_{ds} indicating ohmic source and drain contacts; the I_{ds}–V_g curves also show that I_{ds} increases as the gate voltage V_g decreases from 0 to −1 V representing a p-type enhancement-mode FET. In comparison with BP transistors (Fig. 5(b)), the turn on threshold voltage (of V_g) for lithium-intercalated BP transistors (Fig. 5(d)) shifts slightly towards negative voltage, consistent with hole accumulation resulted from p-type doping by lithium intercalation.

To achieve n-type FETs, we create n-type doping by using zero-valent Cu for intercalation. We use tetrakis (acetonitrile) copper (I) hexafluorophsphate precursor in mix with acetone (1 mg: 5 mL) and BP samples at 45 °C for 40 minutes to enable sufficient intercalation [73]. The samples are then washed with acetone and dried for transistor fabrication. The I_{ds}–V_{ds} and I_{ds}–V_g curves are measured for the Cu intercalated device (Figs. 5(e) and 5(f)). The I_{ds}–V_{ds} shows linear curve indicating ohmic contact; the I_{ds}–V_g curves show that I_{ds} increases as the gate voltage V_g increases from −2 V to positive voltage, representing an n-type depletion-mode FET. Note that in comparison with p-type devices, the Cu-intercalated device has a higher electrical resistance, possibly due to lower electron carrier density when converted from p- to n-type doping.

It is interesting to note that an increase in mobility after intercalation is observed. In general, a reduction in carrier mobility is expected for common semiconductors due to stronger impurity scattering. Here, the lithium intercalated BP samples retain p-type characteristics for different concentrations, but the hole mobility is measured to be ~ 380 $cm^2/(V{\cdot}s)$ for pristine BP and increases to ~ 820 $cm^2/(V{\cdot}s)$ for $Li_{0.3}P$. To better

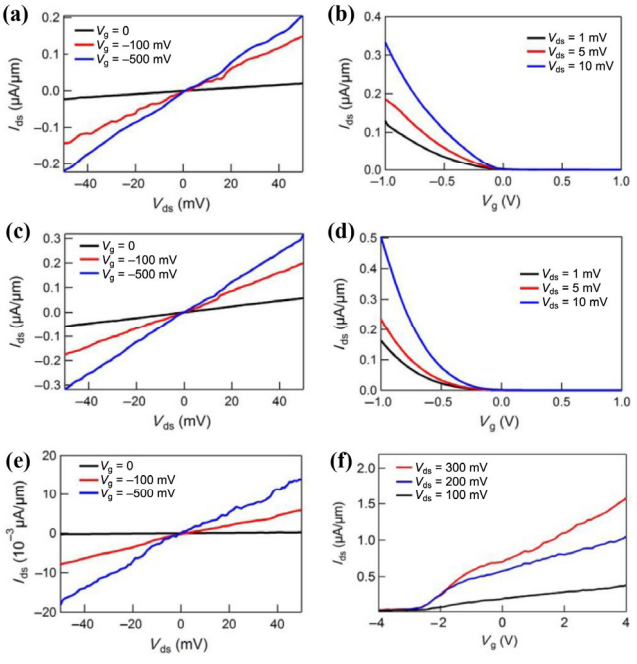

Figure 5 Complementary field-effect transistors (FETs). ((a), (c), (e)) I_{ds}–V_{ds} data for FET devices based on BP, $Li_{0.2}P$, and CuP, respectively. ((b), (d), (f)) I_{ds}–V_g data for FET devices based on BP, $Li_{0.2}P$, and CuP, respectively. The former two devices represent p-type enhancement-mode FET, while the latter device represents n-type depletion-mode FET.

understand this phenomenon, we perform *ab initio* calculation of the band structure, density of states, and mobility for intercalated BP. The electronic band structures are calculated using density functional theory [74–79] and shows a direct gap of 0.18 eV at Z point for bulk BP (Fig. 6(a)). Both the valence bands and conduction bands are mainly contributed by the p and s orbitals of P atoms. When Li ion is intercalated into BP, the Fermi level is shifted to the bottom of the conduction band, resulting in a p-type doping trend. The calculated density of states (DOS) shows that Li^+ does not significantly change the overall DOS since the main contribution to the total DOS is located in the deep valance band. For Cu intercalation, the Fermi level shifts to the conduction band resulting in n-type doing. The Cu 3d states are hybridized with P 3p states at the top of the valence band. A small proportion of Cu 3d electrons will couple with the conduction bands. These hybridized states around the Fermi level are partly filled. To study the effects of intercalation on the charge mobility, we constructed *ab-initio* electronic transport model with explicit solution to the linearized Boltzmann transport equation [80, 81]. The mobility is obtained from [82]

$$\mu = \frac{1}{3}\frac{\int v(k)\left(\frac{k}{\pi}\right)^2\left(\frac{g}{E}\right)\mathrm{d}k}{\int\left(\frac{k}{\pi}\right)^2 f\mathrm{d}k} \quad (1)$$

Here, E is electric field, and v (k) is the electron group velocity. f and g are electron distribution and perturbation to the electron distribution, respectively, which can be solved explicitly from Boltzmann transport equation with relaxation time approximation considering several scattering mechanisms

$$\nu_{el}(k) = \nu_{ii}(k) + \nu_{pe(k)} + \nu_{de}(k) + \nu_{dis}(k) \quad (2)$$

where ν_{el}, ν_{ii}, ν_{pe}, ν_{de}, and ν_{dis} stand for the elastic, ionized impurity, piezoelectric, deformation potential, and dislocation scattering rates, respectively. The presence of electrical neutral impurity (such as oxygen and water) can lead to defect scattering

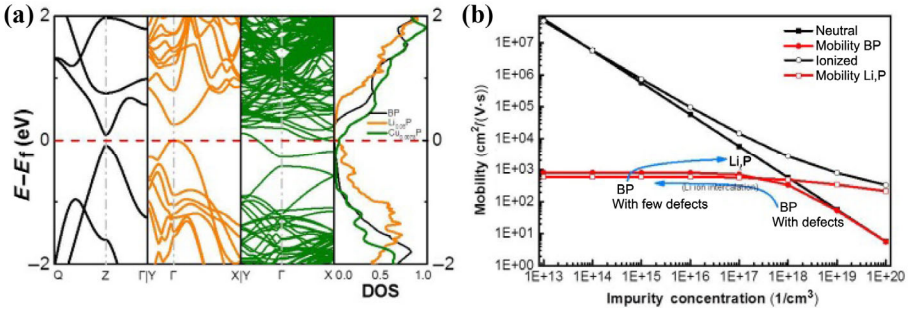

Figure 6 Electronic band structures and charge mobility by density functional theory (DFT) calculations. (a) Band structures and density of states (DOS) calculated for different ionic concentrations. Fermi level shift confirms p-type doping under lithium intercalation and n-type doping under Cu intercalation respectively, in consistency with the experimental observations. (b) Effects to carrier mobility from different scattering mechanisms including neutral impurity scattering and ionized impurity scattering. The competing effects result in an overall mobility enhancement during the intercalation.

in addition to natural p-type dopants (such as Sn during growth) [83]. When the neutral impurity has a concentration higher than 10^{17} cm^{-3}, the calculation results of Fig. 6(b) show that impurity scattering will significantly reduce the mobility of BP. For example, the hole mobility decreases from 816 to 336 $cm^2/(V·s)$ when the impurity concentration reaches 10^{18} cm^{-3}. Although ionization leads to more impurity during lithium intercalation, the ionized impurity scattering can be relatively weaker in comparison with neutral impurity scattering due to the large 2D interlayer spacing and unique phase structures of Li_xP. Thus, we attribute the mobility enhancement to the suppressed neutral impurity after intercalation. Note that literature shows that increased hole mobility with addition of Li^+ dopant is not an isolated case in semiconductor materials. The improvement due to p-type doping has been reported and investigated for organic semiconductor [84] and oxide materials [85]. Previous study found that the effect is related to the existence of intermediate trap sites in the host crystal [86]. Trap sites are localized energy states within the bandgap that came from defects in the material. Excited carriers can fall into the trap sites instead of into the conduction band, thus reducing the overall mobility. Intercalation increases the number of carriers and fills up the trap sites, effectively increasing carrier mobility and conductivity.

4 Conclusion

In summary, we have demonstrated complementary doping of 2D materials using ionic intercalations to achieve p-type and n-type transistors, as well as diode devices. Through the anisotropic transport study, we show that widely tunable electrical properties of black phosphorus can be achieved with high device stability and performance. In addition, mobility enhancement through ionic doping is observed for lithium intercalated BP and verified using density functional theory based *ab initio* calculations based on density functional theory. Our study provides a generic routine to control 2D building blocks with precise and local doping to achieve monolithic circuits and advanced functionalities. More generally, further extending the diversity of 2D host materials, dopants, in combination with modern semiconductor processing, this approach could open up many new opportunities through the rational design of nanomaterials with atomic-level control.

Acknowledgements

Y. H. acknowledges support from a CAREER award from the National Science Foundation under grant DMR-1753393, an Alfred P. Sloan Research Fellowship under grant FG-2019-11788, a Young Investigator Award from the US Air Force Office of Scientific Research under grant FA9550-17-1-0149, a Doctoral New Investigator Award from the American Chemical Society Petroleum Research Fund under grant 58206-DNI5, as well as from the UCLA Sustainable LA Grand Challenge and the Anthony and Jeanne Pritzker Family Foundation. This work used the Extreme Science and Engineering Discovery Environment (XSEDE), which is supported by National Science Foundation grant number ACI-1548562. Specifically, it used the Bridges system, which is supported by NSF award number ACI-1445606, at the Pittsburgh Supercomputing Center (PSC).

References

[1] Lieber, C. M. Nanoscale science and technology: Building a big future from small things. *MRS Bull*. **2003**, *28*, 486–491.
[2] Morales, A. M.; Lieber, C. M. A laser ablation method for the synthesis of crystalline semiconductor nanowires. *Science* **1998**, *279*, 208–211.
[3] Cui, Y.; Wei, Q. Q.; Park, H.; Lieber, C. M. Nanowire nanosensors for highly sensitive and selective detection of biological and chemical species. *Science* **2001**, *293*, 1289–1292.
[4] Duan, X. F.; Huang, Y.; Cui, Y.; Wang, J. F.; Lieber, C. M. Indium phosphide nanowires as building blocks for nanoscale electronic and optoelectronic devices. *Nature* **2001**, *409*, 66–69.
[5] Huang, Y.; Duan, X. F.; Cui, Y.; Lauhon, L. J.; Kim, K. H.; Lieber, C. M. Logic gates and computation from assembled nanowire building blocks. *Science* **2001**, *294*, 1313–1317.
[6] Xiang, J.; Lu, W.; Hu, Y. J.; Wu, Y.; Yan, H.; Lieber, C. M. Ge/Si nanowire heterostructures as high-performance field-effect transistors. *Nature* **2006**, *441*, 489–493.
[7] Hu, Y. J.; Xiang, J.; Liang, G.; Yan, H.; Lieber, C. M. Sub-100 nanometer channel length Ge/Si nanowire transistors with potential for 2 THz switching speed. *Nano Lett*. **2008**, *8*, 925–930.
[8] Hu, Y. J.; Churchill, H. O. H.; Reilly, D. J.; Xiang, J.; Lieber, C. M.; Marcus, C. M. A Ge/Si heterostructure nanowire-based double quantum dot with integrated charge sensor. *Nat. Nanotechnol*. **2007**, *2*, 622–625.
[9] Yan, H.; Choe, H. S.; Nam, S. W.; Hu, Y. J.; Das, S.; Klemic, J. F.; Ellenbogen, J. C.; Lieber, C. M. Programmable nanowire circuits for nanoprocessors. *Nature* **2011**, *470*, 240–244.
[10] Hu, Y. J.; Kuemmeth, F.; Lieber, C. M.; Marcus, C. M. Hole spin relaxation in Ge-Si core-shell nanowire qubits. *Nat. Nanotechnol*. **2012**, *7*, 47–50.
[11] Dai, H. J.; Wong, E. W.; Lieber, C. M. Probing electrical transport in nanomaterials: conductivity of individual carbon nanotubes. *Science* **1996**, *272*, 523–526.
[12] Wong, E. W.; Sheehan, P. E.; Lieber, C. M. Nanobeam mechanics: Elasticity, strength, and toughness of nanorods and nanotubes. *Science* **1997**, *277*, 1971–1975.
[13] Odom, T. W.; Huang, J. L.; Kim, P.; Lieber, C. M. Atomic structure and electronic properties of single-walled carbon nanotubes. *Nature* **1998**, *391*, 62–64.
[14] Hu, J. T.; Odom, T. W.; Lieber, C. M. Chemistry and physics in one dimension: Synthesis and properties of nanowires and nanotubes.

Acc. Chem. Res. **1999**, *32*, 435–445.
[15] Kim, P.; Odom, T. W.; Huang, J. L.; Lieber, C. M. Electronic density of states of atomically resolved single-walled carbon nanotubes: Van hove singularities and end states. *Phys. Rev. Lett.* **1999**, *82*, 1225–1228.
[16] Rueckes, T.; Kim, K.; Joselevich, E.; Tseng, G. Y.; Cheung, C. L.; Lieber, C. M. Carbon nanotube-based nonvolatile random access memory for molecular computing. *Science* **2000**, *289*, 94–97.
[17] Avouris, P. Molecular electronics with carbon nanotubes. *Acc. Chem. Res.* **2002**, *35*, 1026–1034.
[18] McEuen, P. L.; Fuhrer, M. S.; Park, H. Single-walled carbon nanotube electronics. *IEEE Trans. Nanotechnol.* **2002**, *1*, 78–85.
[19] Kong, J.; Franklin, N. R.; Zhou, C. W.; Chapline, M. G.; Peng, S.; Cho, K.; Dai, H. J. Nanotube molecular wires as chemical sensors. *Scienc* **2000**, *287*, 622–626.
[20] Dresselhaus, M. S.; Dresselhaus, G.; Eklund, P. C.; Rao, A. M. Carbon nanotubes. In *The Physics of Fullerene-Based and Fullerene-Related Materials*; Andreoni, W., Ed.; Springer: Dordrecht, 2000; pp 331–379.
[21] Kelty, S. P.; Chen, C. C.; Lieber, C. M. Superconductivity at 30 K in caesium-doped C_{60}. *Nature* **1991**, *352*, 223–225.
[22] Chen, C. C.; Lieber, C. M. Isotope effect and superconductivity in metal-doped C_{60}. *Science* **1993**, *259*, 655–658.
[23] Zhang, J.; Liu, J.; Huang, J. L.; Kim, P.; Lieber, C. M. Creation of nanocrystals through a solid-solid phase transition induced by an STM tip. *Science* **1996**, *274*, 757–760.
[24] Dekker, C.; Tans, S. J.; Geerligs, L. J.; Bezryadin, A.; Wu, J.; Wegner, G.. Towards electrical transport on single molecules. In *Atomic and Molecular Wires*; Joachim, C.; Roth, S., Eds.; Kluwer Academic Publisher: Boston, 1997.
[25] Liu, J.; Dai, H. J.; Hafner, J. H.; Colbert, D. T.; Smalley, R. E.; Tans, S. J.; Dekker, C. Fullerene "crop circles". *Nature* **1997**, *385*, 780–781.
[26] Liu, J.; Rinzler, A. G.; Dai, H. J.; Hafner, J. H.; Bradley, R. K.; Boul, P. J.; Lu, A.; Iverson, T.; Shelimov, K.; Huffman, C. B. et al. Fullerene pipes. *Science* **1998**, *280*, 1253–1256.
[27] Kelty, S. P.; Lieber, C. M. Scanning tunneling microscopy investigations of the electronic structure of potassium-graphite intercalation compounds. *J. Phys. Chem.* **1989**, *93*, 5983–5985.
[28] Kelty, S. P.; Lieber, C. M. Atomic-resolution scanning-tunneling-microscopy investigations of alkali-metal-graphite intercalation compounds. *Phys. Rev. B* **1989**, *40*, 5856–5859.
[29] Wang, C.; He, Q. Y.; Halim, U.; Liu, Y. Y.; Zhu, E. B.; Lin, Z. Y.; Xiao, H.; Duan, X. D.; Feng, Z. Y.; Cheng, R. et al. Monolayer atomic crystal molecular superlattices. *Nature* **2018**, *555*, 231–236.
[30] Lieber, C. Modification and manipulation of layered materials using scanned probe microscopies. In *Proceedings of the SPIE 10310, Technology of Proximal Probe Lithography*, Bellingham, USA, 1993, p 103100D.
[31] Zhang, Y. B.; Tan, Y. W.; Stormer, H. L.; Kim, P. Experimental observation of the quantum hall effect and berry's phase in graphene. *Nature* **2005**, *438*, 201–204.
[32] Li, X. L.; Wang, X. R.; Zhang, L.; Lee, S.; Dai, H. J. Chemically derived, ultrasmooth graphene nanoribbon semiconductors. *Science* **2008**, *319*, 1229–1232.
[33] Park, J. U.; Nam, S. W.; Lee, M. S.; Lieber, C. M. Synthesis of monolithic graphene–graphite integrated electronics. *Nat. Mater.* **2012**, *11*, 120–125.
[34] Butler, S. Z.; Hollen, S. M.; Cao, L. Y.; Cui, Y.; Gupta, J. A.; Gutierrez, H. R.; Heinz, T. F.; Hong, S. S.; Huang, J. X.; Ismach, A. F. et al. Progress, challenges, and opportunities in two-dimensional materials beyond graphene. *ACS Nano* **2013**, *7*, 2898–2926.
[35] Gao, N.; Gao, T.; Yang, X.; Dai, X. C.; Zhou, W.; Zhang, A. Q.; Lieber, C. M. Specific detection of biomolecules in physiological solutions using graphene transistor biosensors. *Proc. Natl. Acad. Sci. USA* **2016**, *113*, 14633–14638.
[36] Novoselov, K. S.; Jiang, D.; Schedin, F.; Booth, T. J.; Khotkevich, V. V.; Morozov, S. V; Geim, A. K. Two-dimensional atomic crystals. *Proc. Natl. Acad. Sci. USA* **2005**, *102*, 10451–10453.
[37] Kang, J. S.; Wu, H.; Li, M.; Hu, Y. J. Intrinsic low thermal conductivity and phonon renormalization due to strong anharmonicity of single-crystal tin selenide. *Nano Lett.* **2019**, *19*, 4941–4948.
[38] Novoselov, K. S.; Mishchenko, A.; Carvalho, A.; Castro Neto, A. H. 2D materials and van der waals heterostructures. *Science* **2016**, *353*, aac9439.
[39] Liu, Y.; Weiss, N. O.; Duan, X. D.; Cheng, H. C.; Huang, Y.; Duan, X. F. Van der waals heterostructures and devices. *Nat. Rev. Mater.* **2016**, *1*, 16042.
[40] Tan, C. L.; Cao, X. H.; Wu, X. J.; He, Q. Y.; Yang, J.; Zhang, X.; Chen, J. Z.; Zhao, W.; Han, S. K.; Nam, G. H. et al. Recent advances in ultrathin two-dimensional nanomaterials. *Chem. Rev.* **2017**, *117*, 6225–6331.
[41] Wang, X. R.; Li, X. L.; Zhang, L.; Yoon, Y.; Weber, P. K.; Wang, H. L.; Guo, J.; Dai, H. J. N-doping of graphene through electrothermal reactions with ammonia. *Science* **2009**, *324*, 768–771.
[42] Lei, S. D.; Wang, X. F.; Li, B.; Kang, J. H.; He, Y. M.; George, A.; Ge, L. H.; Gong, Y. J.; Dong, P.; Jin, Z. H. et al. Surface functionalization of two-dimensional metal chalcogenides by lewis acid-base chemistry. *Nat. Nanotechnol.* **2016**, *11*, 465–471.
[43] Liu, H. T.; Liu, Y. Q.; Zhu, D. B. Chemical doping of graphene. *J. Mater. Chem.* **2011**, *21*, 3335–3345.
[44] Wang, H. T.; Wang, Q. X.; Cheng, Y. C.; Li, K.; Yao, Y. B.; Zhang, Q.; Dong, C. Z.; Wang, P.; Schwingenschlögl, U.; Yang, W. et al. Doping monolayer graphene with single atom substitutions. *Nano Lett.* **2012**, *12*, 141–144.
[45] Li, H. L.; Wu, X. P.; Liu, H. J.; Zheng, B. Y.; Zhang, Q. L.; Zhu, X. L.; Wei, Z.; Zhuang, X. J.; Zhou, H.; Tang, W. X. et al. Composition-modulated two-dimensional semiconductor lateral heterostructures via layer-selected atomic substitution. *ACS Nano* **2017**, *11*, 961–967.
[46] Tsetseris, L.; Wang, B.; Pantelides, S. T. Substitutional doping of graphene: The role of carbon divacancies. *Phys. Rev. B* **2014**, *89*, 035411.
[47] Xu, X. D.; Gabor, N. M.; Alden, J. S.; van der Zande, A. M.; Mceuen, P. L. Photo-thermoelectric effect at a graphene interface junction. *Nano Lett.* **2010**, *10*, 562–566.
[48] Pospischil, A.; Furchi, M. M.; Mueller, T. Solar-energy conversion and light emission in an atomic monolayer p–n diode. *Nat. Nanotechnol.* **2014**, *9*, 257–261.
[49] Baugher, B. W. H.; Churchill, H. O. H.; Yang, Y. F.; Jarillo-herrero, P. Optoelectronic devices based on electrically tunable p–n diodes in a monolayer dichalcogenide. *Nat. Nanotechnol.* **2014**, *9*, 262–267.
[50] Geim, A. K.; Grigorieva, I. V. Van der waals heterostructures. *Nature* **2013**, *499*, 419–425.
[51] Huang, C. M.; Wu, S. F.; Sanchez, A. M.; Peters, J. J. P.; Beanland, R.; Ross, J. S.; Rivera, P.; Yao, W.; Cobden, D. H.; Xu, X. D. Lateral heterojunctions within monolayer $MoSe_2$–WSe_2 semiconductors. *Nat. Mater.* **2014**, *13*, 1096–1101.
[52] Gong, Y. J.; Lin, J. H.; Wang, X. L.; Shi, G.; Lei, S. D.; Lin, Z.; Zou, X. L.; Ye, G. L.; Vajtai, R.; Yakobson, B. I. et al. Vertical and in-plane heterostructures from WS_2/MoS_2 monolayers. *Nat. Mater.* **2014**, *13*, 1135–1142.
[53] Duan, X. D.; Wang, C.; Shaw, J. C.; Cheng, R.; Chen, Y.; Li, H. L.; Wu, X. P.; Tang, Y.; Zhang, Q. L.; Pan, A. L. et al. Lateral epitaxial growth of two-dimensional layered semiconductor heterojunctions. *Nat. Nanotechnol.* **2014**, *9*, 1024–1030.
[54] Li, M.; Kang, J. S.; Nguyen, H. D.; Wu, H.; Aoki, T.; Hu, Y. J. Anisotropic thermal boundary resistance across 2D black phosphorus: Experiment and atomistic modeling of interfacial energy transport. *Adv. Mater.* **2019**, *31*, 1901021.
[55] Kang, J. S.; Ke, M.; Hu, Y. J. Ionic intercalation in two-dimensional van der waals materials: *In situ* characterization and electrochemical control of the anisotropic thermal conductivity of black phosphorus. *Nano Lett.* **2017**, *17*, 1431–1438.
[56] Morita, A. Semiconducting black phosphorus. *Appl. Phys. A* **1986**, *39*, 227–242.
[57] Ling, X.; Wang, H.; Huang, S. X.; Xia, F. N.; Dresselhaus, M. S. The renaissance of black phosphorus. *Proc. Natl. Acad. Sci. USA* **2015**, *112*, 4523–4530.
[58] Li, M.; Kang, J. S.; Hu, Y. J. Anisotropic thermal conductivity measurement using a new asymmetric- beam time-domain thermoreflectance (AB-TDTR) method. *Rev. Sci. Instrum.* **2018**, *89*, 084901.
[59] Sugai, S.; Shirotani, I. Raman and infrared reflection spectroscopy in black phosphorus. *Solid State Commun.* **1985**, *53*, 753–755.
[60] Wu, J. X.; Mao, N. N.; Xie, L. M.; Xu, H.; Zhang, J. Identifying the crystalline orientation of black phosphorus using angle-resolved

polarized Raman spectroscopy. *Angew. Chem., Int. Ed.* **2015**, *54*, 2366–2369.

[61] Zhao, S. J.; Kang, W.; Xue, J. M. The potential application of phosphorene as an anode material in Li-ion batteries. *J. Mater. Chem. A* **2014**, *2*, 19046–19052.

[62] Li, Q. F.; Duan, C. G.; Wan, X. G.; Kuo, J. L. Theoretical prediction of anode materials in Li-ion batteries on layered black and blue phosphorus. *J. Phys. Chem. C* **2015**, *119*, 8662–8670.

[63] Jung, S. C.; Han, Y. K. Thermodynamic and kinetic origins of lithiation-induced amorphous-to-crystalline phase transition of phosphorus. *J. Phys. Chem. C* **2015**, *119*, 12130–12137.

[64] Shirotani, I. Growth of large single crystals of black phosphorus at high pressures and temperatures, and its electrical properties. *Mol. Cryst. Liq. Cryst.* **1982**, *86*, 203–211.

[65] Montgomery, H. C. Method for measuring electrical resistivity of anisotropic materials. *J. Appl. Phys.* **1971**, *42*, 2971–2975.

[66] Akahama, Y.; Endo, S.; Narita, S. Electrical properties of single-crystal black phosphorus under pressure. *Phys. B+C* **1986**, *139–140*, 397–400.

[67] Akahama, Y.; Endo, S.; Narita, S. I. Electrical properties of black phosphorus single crystals. *J. Phys Soc. Jpn.* **1983**, *52*, 2148–2155.

[68] Gong, Y. J.; Yuan, H. T.; Wu, C. L.; Tang, P. Z.; Yang, S. Z.; Yang, A. K.; Li, G. D.; Liu, B. F.; van de Groep, J.; Brongersma, M. L. et al. Spatially controlled doping of two-dimensional SnS_2 through intercalation for electronics. *Nat. Nanotechnol.* **2018**, *13*, 294–299.

[69] Xiong, F.; Wang, H. T.; Liu, X. G.; Sun, J.; Brongersma, M.; Pop, E.; Cui, Y. Li intercalation in MoS_2: *In situ* observation of its dynamics and tuning optical and electrical properties. *Nano Lett.* **2015**, *15*, 6777–6784.

[70] Ashcroft, N. W.; Mermin, N. D. *Solid State Physics*; Holt, Rinehart & Winston: New York, 1976.

[71] Nguyen, H. D.; Kang, J. S.; Li, M.; Hu, Y. J. High-performance field emission based on nanostructured tin selenide for nanoscale vacuum transistors. *Nanoscale* **2019**, *11*, 3129–3137.

[72] Brovman, Y. M.; Small, J. P.; Hu, Y. J.; Fang, Y.; Lieber, C. M.; Kim, P. Electric field effect thermoelectric transport in individual silicon and germanium / silicon nanowires. *J. Appl. Phys.* **2016**, *119*, 234304.

[73] Koski, K. J.; Cha, J. J.; Reed, B. W.; Wessells, C. D.; Kong, D. S.; Cui, Y. High-density chemical intercalation of zero-valent copper into Bi_2Se_3 nanoribbons. *J. Am. Chem. Soc.* **2012**, *134*, 7584–7587.

[74] Giannozzi, P.; Baroni, S.; Bonini, N.; Calandra, M.; Car, R.; Cavazzoni, C.; Ceresoli, D.; Chiarotti, G. L.; Cococcioni, M.; Dabo, I. et al. QUANTUM ESPRESSO: A modular and open-source software project for quantum simulations of materials. *J. Phys. Condens. Matter* **2009**, *21*, 395502.

[75] Giannozzi, P.; Andreussi, O.; Brumme, T.; Bunau, O.; Buongiorno Nardelli, M.; Calandra, M.; Car, R.; Cavazzoni, C.; Ceresoli, D.; Cococcioni, M. et al. Advanced capabilities for materials modelling with quantum ESPRESSO. *J. Phys. Condens. Matter* **2017**, *29*, 465901.

[76] Fan, H.; Wu, H.; Lindsay, L.; Hu, Y. J. *Ab initio* investigation of single-layer high thermal conductivity boron compounds. *Phys. Rev. B* **2019**, *100*, 085420.

[77] Kang, J. S.; Li, M.; Wu, H.; Nguyen, H.; Hu, Y. J. Experimental observation of high thermal conductivity in boron arsenide. *Science* **2018**, *361*, 575–578.

[78] Kang, J. S.; Wu, H.; Hu, Y. J. Thermal properties and phonon spectral characterization of synthetic boron phosphide for high thermal conductivity applications. *Nano Lett.* **2017**, *17*, 7507–7514.

[79] Kang, J. S.; Li, M.; Wu, H.; Nguyen, H.; Hu, Y. J. Basic physical properties of cubic boron arsenide. *Appl. Phys. Lett.* **2019**, *115*, 122103.

[80] Faghaninia, A.; Ager III, J. W.; Lo, C. S. *Ab initio* electronic transport model with explicit solution to the linearized boltzmann transport equation. *Phys. Rev. B* **2015**, *91*, 235123.

[81] Faghaninia, A.; Ager III, J. W.; Lo, C. S. *Ab Initio Model for Mobility and Seebeck Coefficient Using Boltzmann Transport* (*AMoBT*) *Equation* [Online]. NanoHUB. https://nanohub.org/resources/amobt (accessed Nov 27, 2019).

[82] Ziman, J. M. *Electrons and Phonons*: *The Theory of Transport Phenomena in Solids*; Clarendon Press: Oxford, 1960.

[83] Carvalho, A.; Wang, M.; Zhu, X.; Rodin, A. S.; Su, H. B.; Castro Neto, A. H. Phosphorene: From theory to applications. *Nat. Rev. Mater.* **2019**, *1*, 16061.

[84] Maennig, B.; Pfeiffer, M.; Nollau, A.; Zhou, X.; Leo, K.; Simon, P. Controlled P-type doping of polycrystalline and amorphous organic layers: Self-consistent description of conductivity and field-effect mobility by a microscopic percolation model. *Phys. Rev. B* **2001**, *64*, 195208.

[85] Ryu, Y. R.; Lee, T. S.; White, H. W. Properties of arsenic-doped p-type ZnO grown by hybrid beam deposition. *Appl. Phys. Lett.* **2003**, *83*, 87–89.

[86] Snaith, H. J.; Grätzel, M. Enhanced charge mobility in a molecular hole transporter via addition of redox inactive ionic dopant: Implication to dye-sensitized solar cells. *Appl. Phys. Lett.* **2006**, *89*, 262114.